Macromolecules

pubs.acs.org/Macromolecules

Article

Tuning the Effective Interactions between Spherical Double-Stranded DNA Brushes

Ivany C. Romero-Sanchez, Laura E. Castellano, and Marco Laurati*

Cite This: *Macromolecules* 2022, 55, 4459−4468

Read Online

ACCESS | Metrics & More | Article Recommendations | Supporting Information

ABSTRACT: We present an experimental investigation of the mechanisms that can be used to control blunt-end induced effective attractions between densely packed spherical double-stranded DNA (dsDNA) brushes. Using microscopy and particle tracking, we determine the effects of varying the parameters controlling the brush and dsDNA fragment conformation, in particular functionality, salinity, and dsDNA fragment length. The analysis of the structure and dynamics of increasingly concentrated dispersions reveals that a decrease in functionality or an increase in salt content leads to a progressive reduction of the effective attractions. For the functionality, this can be associated with the reduction of the surface density of blunt-end, while for the salinity, this can be associated with DNA backfolding. We, therefore, reveal means of controlling blunt-end-induced interactions that could be used to guide colloidal self-assembly based on DNA base stacking, a parallel platform to base pairing.

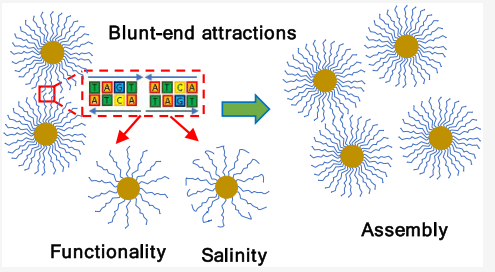

INTRODUCTION

The complex and programmable interactions between DNA fragments have been exploited in the last decades in nanotechnology:[1,2] as a tool to assemble inorganic nanostructures, such as metals, nanoparticles, and nanowires[3] with applications in electronics,[4] optics,[5,6] and sensors;[7] to develop innovative drug delivery systems,[8] with greater ability to penetrate into cells,[9−11] silence gene expression,[12] and perform selective delivery;[13] and to mimic protein-membrane activity in conjunction with lipids in synthetic biology.[14,15] Different interactions can be distinguished and used to control DNA assembly: single-stranded overhangs, also called sticky ends, are short sequences of unpaired nucleotides in the end of longer dsDNA fragments. They can bind to complementary overhangs, driving assembly through Watson−Crick pairing;[16] alternatively, long scaffold single-stranded DNA (ssDNA) can be folded into desired patterns (DNA origami)[17] or DNA bricks with predesigned patterns[18] can be assembled; supramolecular interactions provide additional, orthogonal assembly possibilities,[19] making use of hydrophobic moieties[20] or blunt-end base stacking.[21] Different from sticky ends, blunt-end corresponds to a dsDNA fragment in which both ends are base-paired. However, when the blunt-end of different dsDNA fragments approach each other at a small distance, complementary bases of the dsDNA ends can attract each other. Stacking of short, rigid dsDNA fragments is induced by such interactions.[22]

Beyond DNA nanostructures, the properties of DNA interactions can be exploited to direct the assembly of colloidal particles in a programmable manner.[23,24] Colloids grafted with DNA strands can be assembled selectively through sticky end hybridization; the presence of many sticky ends on the surface of a colloidal particle leads to multivalency and therefore to an effective short-range attractive interaction. Sticky DNA-grafted nano- and microparticles have been used to assemble equilibrium one-component[25,26] and two-component crystalline structures[27,28] by controlling temperature, grafting density, and DNA sequences. Additionally, the specificity of DNA interactions allows us to control the structure of DNA-coated nanoparticle aggregates[29,30] and porous gel structures.[31] Much less explored is the use of supramolecular interactions to design colloidal self-assembly, including blunt-end interactions.[32,33] Blunt-end-based attractions appear as a promising opportunity to combine the specificity of DNA interactions associated with base sequences, with the directionality of the stacking associated with the attraction between the terminations of facing dsDNA fragments. Such directionality has been already used to assemble large DNA nanostructures by merging blunt-end stacking and shape selectivity.[21,34−36]

Combining microscopy experiments, theory, and simulations, we recently showed that polymeric microparticles coated with dense, long dsDNA fragments assemble into locally ordered aggregate structures through blunt-end interactions between DNA fragments in contacting brushes.[37] The large local density of blunt-end combined with the stretched configuration of DNA fragments leads to an effective short-

Received: January 28, 2022
Revised: April 11, 2022
Published: May 25, 2022

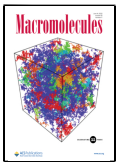

https://doi.org/10.1021/acs.macromol.2c00220
Macromolecules 2022, 55, 4459−4468

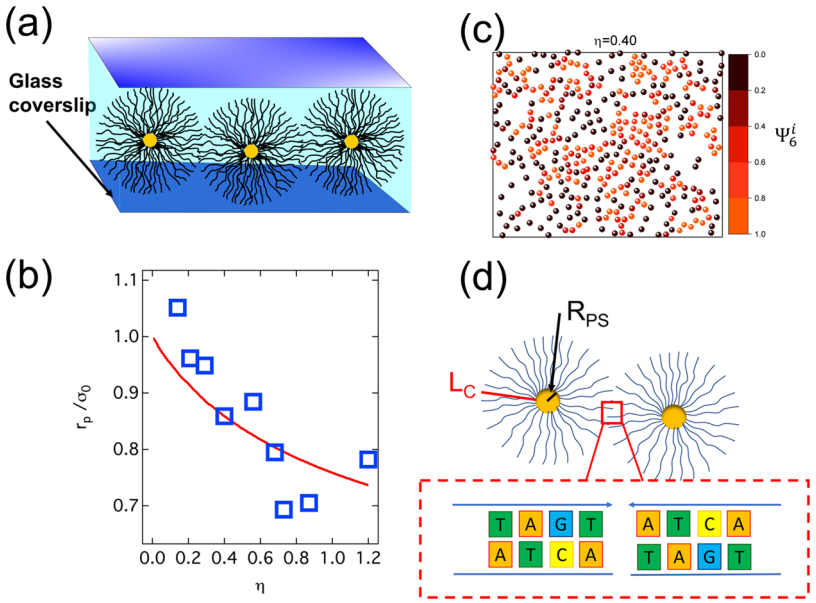

Figure 1. (a) Sketch of the experimental system consisting of dsDNA-grafted PS beads confined in quasi-2D by a glass coverslip and a microscopy slide separated by a 10 μm spacer. (b) Position of the first peak of $g(r)$, r_p, as a function of η, for $f = 1.0 \times 10^5$, $N = 10$ kbp and no added salt (symbols). The line represents the results of theoretical calculations, as described in detail in ref 37. (c) Rendering of sample with $\eta = 0.40$ evidencing the presence of aggregation. The color scale indicates the value of the 6-fold order parameter of each particle. (d) Sketch of attractive interactions between blunt-end (in the zoomed view) of dsDNA chains pertaining to contacting brushes.

range attractive interaction between the colloids, which is in competition with longer-ranged electrostatic repulsion arising from residual charges. In this work, we use microscopy experiments and particle tracking to show that the effective attractive interactions induced by blunt-end between dsDNA-grafted colloids can be tuned by means of precisely controllable parameters, such as concentration of monovalent salt, particle grafting density, and length of the DNA fragments. This is revealed by analyzing the effects of these parameters on the microscopic structure and dynamics of the system. The analysis shows that acting on the density of blunt-end on the brush surface, either through a reduction of functionality or by inducing DNA backfolding through the addition of monovalent salt, the attractions can be reduced until disappearing.

MATERIALS AND METHODS

Samples. The complete procedure to obtain colloidal beads grafted with long dsDNA fragments was described in previous work.[38,39] The main steps of the procedure can be summarized as follows: (i) Synthesis of 10 or 20 kbp dsDNA using polymerase chain reaction (PCR) to amplify end-biotinylated fragments. (ii) Grafting of DNA fragments onto the surface of polystyrene (PS) beads (radius $R_{PS} = 0.49$ μm, Bangs Laboratories) functionalized with streptavidin. In step (i), the end-biotinylated dsDNA fragments were amplified using λ-DNA as a template (New England Biolabs) and a DNA polymerase enzyme as part of the Go Taq Long PCR Master Mix (Promega). The PCR protocols accompanied with this product were followed in the amplification process. The dsDNA fragments' end-functionalization was performed by PCR using reverse and forward primers, which were synthesized and HPLC-purified at IDT. In more detail, the forward primer was 5′-biotinylated and included an extended 15-atom spacer tetra-ethylene-glycol (TEG), which has the effect of reducing steric hindrance and therefore increasing the binding efficiency of the long dsDNA to the streptavidin-functionalized PS beads. The reverse primers were not modified. Grafting was obtained using a binding buffer (Dynabeads Kilobase binder Kit, Invitrogen). Biotin end-modified dsDNA fragments were mixed in appropriate amounts with the PS beads suspension to achieve a final volume of about 35 μL and incubated at room temperature under gentle rotation for 12 h to avoid sedimentation. The unreacted dsDNA fragments were washed out using sequential washes with Milli-Q water. This was achieved by centrifuging the suspension and by pipetting off the supernatant. The DNA-grafted beads were finally redispersed into 40 μL of Milli-Q water. The procedure was repeated three times. The number of grafted dsDNA chains per bead (functionality f) was quantified from the number of the beads (value that was determined from the concentration of the stock bead solution) and the number of DNA chains in the reaction bottle before the cleaning procedure. The DNA concentration was determined by measuring the absorbance at 260 nm employing a micro-volume spectrometer (MicroDrop, Thermo Scientific). Grafted particles were then dispersed in deionized water or in a sterile saline solution containing 5.0×10^{-2} M or 1.0 M NaCl. Dispersions with different particle concentrations were obtained by diluting a sediment obtained by centrifugation.

Microscopy. Quasi-two-dimensional (2D) samples were prepared by confining the dispersions between a microscope slide and a coverslip (#1 thickness, 0.15 mm) (Figure 1a): The distance between the slide and coverslip was precisely set by means of a PET-based double-sided tape with thickness $h = 10$ μm (no. 5601, Nitto). Glass surfaces were made hydrophobic through cleaning with a Rain X solution (ITW Krafft) to avoid particles sticking on the glass. After depositing 1.2 μL of sample onto the microscope slide, the coverslip was uniformly pressed against the slide until reaching the desired separation distance and successively glued on the sides using epoxy resin. The microscopy images were acquired on a Nikon Ti−S inverted microscope using a Nikon 50× LWD objective (N.A. 0.9) in bright-field contrast. The choice of this contrast technique instead of fluorescence microscopy is due to the possible damage of labeled DNA fragments induced by prolonged exposure to intense laser illumination.[40] Furthermore, fluorescent labeling of the dsDNA end fragments can modify their interactions, i.e., blunt-end attractions.[41] For each sample, about 50 series of 1000 images of 1280 × 1024 pixels were acquired at different locations in the sample using a 2.2 Mp Pixelink M2 camera at a frame rate of 15 fps. Longer acquisitions were not possible due to stability issues. Particle coordinates were extracted from images employing the Mosaic Suite for Fiji,[42] while particle trajectories were determined using TrackMate.[43] De-drifting

https://doi.org/10.1021/acs.macromol.2c00220
Macromolecules 2022, 55, 4459−4468

procedures available in TrackMate were applied to sample trajectories before calculating the MSDs. To avoid sample degradation, experiments were run shortly after sample loading. The average area packing fraction η of the confined dispersions was determined through the analysis of sample images by particle tracking. For each dispersion, the results of the analysis of 1000 images were averaged.

RESULTS AND DISCUSSION

Reference System: Functionality $f = 1 \times 10^5$, DNA Fragment Length $N = 10$ kbp, and No Salt Added. We report in this section the results obtained for quasi-2D dispersions of particles with functionality $f = 1 \times 10^5$, DNA fragment length $N = 10$ kbp, and no added salt. In the absence of added salt, counterions are absorbed inside the dsDNA brush, resulting in a strong repulsion between neighbor DNA fragments that leads to a fully stretched configuration. For this reason, the brush thickness equals the contour length $L_C = 3.4$ μm, as demonstrated in previous work.[38] This corresponds to a brush-core size ratio $L_C/R_{PS} \approx 6.9$, indicating a star-like architecture of the particles. The results obtained for this system represent a reference for the study of the effects related to the variation of the control parameters of the dispersions, in particular the particle functionality, the monovalent salt content, and the DNA fragment length.

We summarize the detailed investigation described in ref 37, in which microscopy experiments, theory, and simulations were combined to analyze the structure and dynamics of the dispersions: In the absence of added salt, with increasing colloid packing fraction $\eta = n\pi\sigma_0^2/4$, with $n = \langle N_p/A \rangle$ the average particle number surface density calculated using the coordinates obtained from particle tracking, and $\sigma_0 = 2R = 2(R_{PS} + L_C)$ the particle diameter in dilute solution, the DNA brushes deswell (reduce in size). The particle deswelling measured through the minimum interparticle distance r_p (symbols in Figure 1b) extracted from the peak of the radial distribution function $g(r) = N(r)/(2\pi nr\Delta r)$, with $N(r)$ being the number of particles in a thin shell of thickness Δr at distance r from a selected particle, was compared to detailed theoretical calculations (line in Figure 1b). The theory developed in ref 37 describes the brush conformation as a function of increasing packing fraction by considering free energy and entropic contributions: these include the electrostatic interaction between DNA and counterions, the entropic elasticity of the DNA fragments, exclude-volume interactions, the entropic free energy of the noncondensed counterions inside the brush and the free counterions outside the brush, and the osmotic pressure exerted by noncondensed counterions of a brush on neighbor brushes. While these terms act in an antagonistic way, it was found that for thick brushes like those investigated in this work, the osmotic pressure term is particularly important and is responsible for the observed deswelling for increasing packing fraction. Interdigitation of DNA brushes remains always negligible along the deswelling.

In addition, the evolution of the structural arrangement of the dispersions with increasing η was studied through variations in the height and position of the first peak of the $g(r)$, and in the average 6-fold order parameter. This study evidenced the formation of chainlike structures and aggregates at intermediate packing fractions, which can be discerned in the exemplary reconstruction of particle configurations reported in Figure 1c for the sample with $\eta \approx 0.40$, and which can be attributed to the presence of an attractive interaction between the particles. The origin of attractions was attributed to interactions between the blunt-end of contacting brushes[22,44−47] (Figure 1d): when densely grafted brushes are sufficiently packed and the dsDNA fragment conformation is stretched, a condition that is satisfied in the absence of added salt, a sufficiently large number of facing, complementary blunt-end attract each other, leading to an effective attractive potential. The proposed hypothesis about the origin of the attraction was confirmed by the fact that the addition of a small amount of salt, which induces DNA backfolding as demonstrated in ref 38, leads to a strong reduction of the clustering. Furthermore, the local order inside aggregates increases up to a packing fraction $\eta \approx 0.68$, and then suddenly decreases, indicating reentrant ordering. For even larger values of η, the order increases again and finally leads to crystallization. These trends will be recalled in the next session and can be seen in Figure 3, where the first peak height and position, and the average 6-fold order parameter of the reference system are shown as a function of η. Reentrant ordering was explained in terms of a combination between interparticle attraction and particle deswelling: particles form increasingly packed aggregates with increasing η until compression induces a sudden particle deswelling that leads to particle rearrangements and loss of local order. This conclusion was confirmed by simulations, which were able to reproduce the experimental trends by assuming that the spherical brushes interact through a pair potential composed of a short-range attraction and a mild, longer-ranged electrostatic repulsion due to residual charges. A similar reentrance was also observed in the particle dynamics.

In the following sections, we explore how the blunt-end-induced attractive interactions that are present for large functionalities and in the absence of added salt can be modified by variations of these parameters, and additionally of the fragment length.

Since we could not directly determine the variation of the particle size with increasing packing fraction, we use the packing fraction calculated on the basis of the particle size in the dilute limit for comparing samples with different functionalities and salt contents. This corresponds to comparing samples at similar particle number densities.

Effect of Functionality. To explore the effects of varying functionality on the interactions between particles, we compare the structure of dispersions of particles grafted with dsDNA fragments of length $N = 10$ kbp, and having different functionalities $f = 1.0 \times 10^5$, 2.5×10^4, and 5.0×10^3, without any added salt. All considered values of f correspond to dense brushes: if we estimate the grafting density of the particles using the expression $\rho = f/4\pi R_{PS}^2$, which assumes a uniform distribution of grafting points on the surface of the PS bead, we obtain $0.00159 < \rho < 0.031$ fragments/nm^2 and a packing distance $d \approx \rho^{-1/2}$ in the interval $5.7 \lesssim d \lesssim 25$ nm. Additionally, previous experimental evidence[38] obtained under similar conditions indicates that for all explored functionalities, the dsDNA conformation remains fully stretched and the brush size in dilute conditions remains unchanged (we recall that this corresponds to $L_C = 3.4$ μm). We can therefore assume that no significant change in particle softness is induced by changes in the functionality.

Figure 2a,b shows experimentally determined radial distribution functions $g(r)$ for samples with packing fractions $\eta = 0.40$ and 0.68 and the different functionalities investigated. We chose to report the radial distribution functions of dispersions having these packing fractions because in the

https://doi.org/10.1021/acs.macromol.2c00220
Macromolecules 2022, 55, 4459−4468

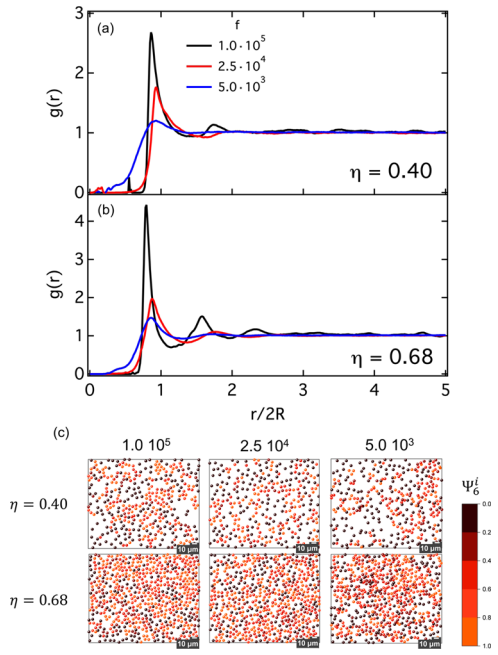

Figure 2. (a, b) Radial distribution functions $g(r)$ for different values of the particle functionality (as indicated) and packing fraction η = 0.40 (a) and 0.68 (b). (c) Renderings of particle positions in samples with η = 0.40 and 0.68 and different functionalities (as indicated). The particle color represents the value of the 6-fold order parameter, as indicated by the color scale.

reference system with $f = 1.0 \times 10^5$, these are the samples that show the most pronounced aggregation phenomena and the presence of a larger degree of local order, i.e., the effects associated with blunt-end attractive interactions. Functions for additional values of η are reported in Figure S1 in the Supporting Information. For $f = 1.0 \times 10^5$, which corresponds to the reference system discussed in the previous section, and η = 0.40 (Figure 2a) chainlike aggregates can be discerned (Figure 2c, top) and $g(r)$ shows a pronounced first peak, at a distance smaller than the diameter of the particles in dilute conditions, and a small second peak. For η = 0.68 (Figure 2b), larger and rounder aggregates are formed and structural heterogeneity is present (Figure 2c, bottom). In ref 37, we demonstrated that the presence of aggregates can be attributed to blunt-end attractions. Additionally, $g(r)$ shows the presence of pronounced peaks. In particular, the first peak, which is observed at approximately $r_0 = 0.82(2R)$, exceeds the value of 4, indicating local crystalline order within the aggregates. The color scale in Figure 2c represents the value of the 6-fold order parameter of particle i, $\Psi_6^i = \frac{1}{N_b}\sum_{j=1}^{N_b} e^{i6\vartheta_{ij}}$, with ϑ_{ij} being the relative orientation angle between particles i and j and N_b being the number of neighbors of particle i. As it can be seen, large values of Ψ_6^i indicate the presence of local hexagonal order within the aggregates.

Decreasing functionality to $f = 2.5 \times 10^4$, the height of the peaks of the $g(r)$ decreases significantly for both values of η: this corresponds to the loss of local order, which is evidenced in snapshots of the samples (Figure 2c, mid column). The number of particles with a large value of the 6-fold order parameter decreases. The peak position is larger than for the reference system but still smaller than the particle diameter in dilute solution. The height of the second peak is also smaller, and the position is found at larger interparticle distances compared to the reference system, supporting the interpretation of the data in terms of the presence of less pronounced aggregation and a more homogeneous structure. For the smallest functionality $f = 5.0 \times 10^3$, a further reduction of the first peak height (Figure 2a,b) and local order (Figure 2c, right column) is observed.

The peak becomes also broader, especially in the region of smaller r values, suggesting that the small grafting density of the particles may allow in this case a small degree of interpenetration of the brushes at a sufficiently large packing fraction, with some particles entangling and forming dimers. The presence of closely connected particles forming dimers can be evinced from the images in Figure 2c. The second peak is also particularly broad and small. The progressive reduction of the height of the first peak of the $g(r)$ and the smaller number of particles presenting a large value of Ψ_6^i with decreasing f indicate that a reduction of functionality leads to a reduction of attraction. This is consistent with a smaller density of blunt-end on the surface of the dsDNA brush corona.

The tendency to a reduced structuring of the dispersions with decreasing f is confirmed at all packing fractions by looking at the values of the height and position of the first peak of $g(r)$, g^{max} and r^{max}, and of the average 6-fold order parameter, $\langle\Psi_6\rangle = \left\langle \frac{1}{N}\sum_{i=1}^{N}\Psi_6^i \right\rangle$, with N the number of particles in an image and $\langle\rangle$ the average over all images acquired for a sample. Figure 3a shows that for $\eta \lesssim 0.7$, the

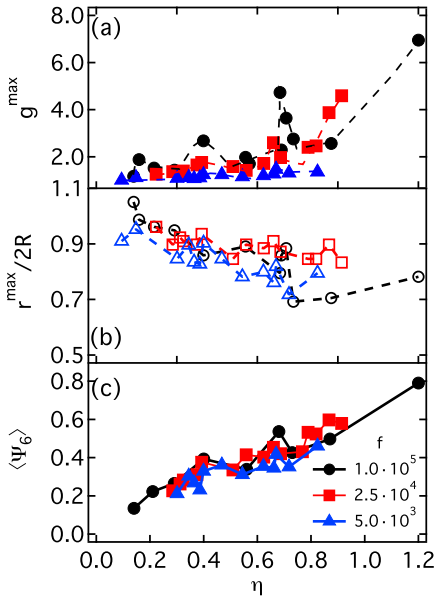

Figure 3. (a) Height and (b) position of the first peak of $g(r)$, and (c) average 6-fold order parameter $\langle\Psi_6\rangle$ as a function of η, for $f = 1.0 \times 10^5$ (circles), $f = 2.5 \times 10^4$ (squares), and $f = 5.0 \times 10^3$ (triangles). Lines in (a) and (b) are a guide to the eye. Error bars are smaller than symbol sizes.

system with $f = 2.5 \times 10^4$ presents smaller values of g^{max}. Still, the largest values of this quantity are observed for η values comparable to those of the reference system. Also, $\langle\Psi_6\rangle$ remains comparable to the reference system. For $f = 5.0 \times 10^3$, the values of g^{max} and also those of $\langle\Psi_6\rangle$ are instead considerably smaller, and in particular, g^{max} shows a much smoother increase as a function of η. The reduction of r^{max}

https://doi.org/10.1021/acs.macromol.2c00220
Macromolecules 2022, 55, 4459−4468

with increasing η becomes less pronounced for $f = 2.5 \times 10^4$, which could be attributed to a reduction in the attractive interaction and associated aggregation, that was inducing additional particle compression. Interestingly, the reduction becomes instead slightly more pronounced than in the reference system for $f = 5.0 \times 10^3$. As also commented in the discussion of Figure 2, this might be due to the small grafting density and thus the possibility that particles interpenetrate.

To investigate the dependence of the dynamics on the particle functionality, we determined the mean-square displacements (MSD), $\Delta r^2(t) = \langle (r_i(t + t_0) - r_i(t_0))^2 \rangle_{t_0,i}$, where r_i is the position of particle i, t is the delay time, t_0 is the time during the particle's trajectory, and $\langle \rangle_{t_0,i}$ indicates an average over all times t_0 and all particles i. Figure 4a,b shows exemplary MSDs

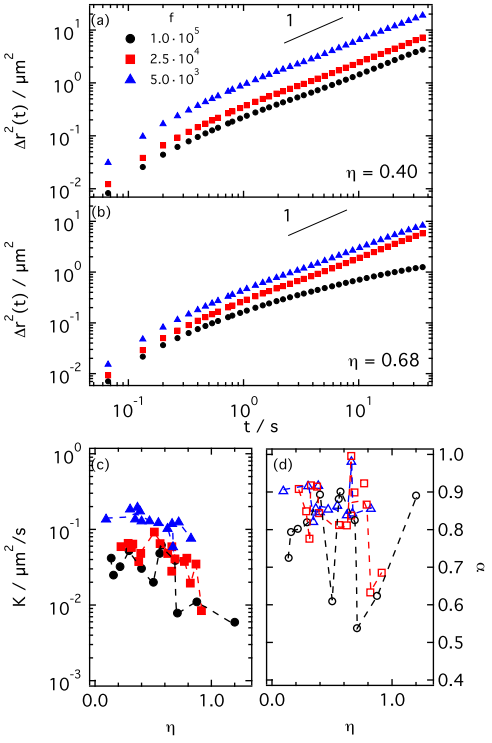

Figure 4. (a, b) Mean-square displacement $\Delta r^2(t)$ for different values of the particle functionality (as indicated) and packing fraction η = 0.40 (a) and 0.68 (b). (c) Effective transport coefficient K as a function of η, for $f = 1.0 \times 10^5$ (circles), $f = 2.5 \times 10^4$ (squares), and $f = 5.0 \times 10^3$ (triangles). (d) Exponent α obtained by fitting the long-time part of the MSD with a power law, $\Delta r^2(t) = 4Kt^\alpha$, as a function of η, same (empty) symbols as in (c).

$\Delta r^2(t)$ obtained for packing fractions η = 0.40 and 0.68 and $f = 1.0 \times 10^5$, 2.5×10^4, and 5.0×10^3. The MSD of samples with additional values of the packing fraction is reported in Figure S2 in the Supporting Information. These MSDs indicate that a decrease in f results in a speedup of the dynamics. The linear dependence of the MSD on delay time at sufficiently long times indicates an approximately diffusive motion. Only in the sample with $\eta = 0.68$ and $f = 1.0 \times 10^5$, a diffusive regime is not attained, which might be associated with the formation of large aggregates, as discussed in the analysis of the microscopic structure. Instead, for $\eta = 0.40$ and $f = 1.0 \times 10^5$, where aggregation is also indicated by the structural analysis, the dynamics remain diffusive. This might be associated with the fact that the small, chainlike clusters that are present in this sample still present a relatively fast translational diffusion. Figure 4c,d reports a transport coefficient K and the exponent α obtained by fitting the long-time part of the MSD according to the equation $\Delta r^2(t) = 4Kt^\alpha$. When $\alpha = 1$, K equals the diffusion coefficient or all functionalities, the transport coefficient K decreases with increasing η, consistent with the progressive crowding of the system. Similar to that observed in the structure, a reentrant behavior is present for $f = 1.0 \times 10^5$ around $\eta = 0.68$, as indicated by a drop in the transport coefficient and the value of α. Values of α significantly smaller than 1 indicate subdiffusive behavior. For $f = 2.5 \times 10^4$, the reentrance is much reduced, especially in K, and it essentially disappears for $f = 5.0 \times 10^3$. The values of K at all packing fractions confirm that the dynamics speed up with decreasing f. The strongest deviations from diffusive behavior are observed for $f = 1.0 \times 10^5$.

In summary, results on the structure and dynamics for different particle functionalities show that aggregation effects observed for the largest value of f progressively reduce with decreasing f until disappearing. This confirms that blunt-end attractions inducing clustering for $f = 1.0 \times 10^5$ is associated with the large functionality, i.e., the high density of blunt-end on the surface of the corona. Since the presence of sufficiently intense attractive interactions inducing aggregation phenomena is intimately responsible for the reentrant ordering observed for $f = 1.0 \times 10^5$, this becomes also less pronounced for $f = 2.5 \times 10^4$ and disappears for $f = 5.0 \times 10^3$. The large grafting density also prevents particle interpenetration, which might become possible for $f = 5.0\ 10^3$ at a sufficiently large packing fraction.

Effect of Monovalent Salt. We investigated the effect of the addition of NaCl to the reference system with $f = 1.0 \times 10^5$ and N = 10 kbp. A previous study[37] investigated the effects of the addition of a concentration c = 0.025 M of NaCl, indicating a strong reduction of aggregation phenomena, which was attributed to a decrease of the blunt-end effective attraction due to dsDNA backfolding that reduces the number of facing blunt-end. Here, we complement these results by investigating additional larger salt concentrations c = 0.05 and 1.00 M. For these concentrations, the size reduction that was determined under dilute conditions in ref 38 and the increased particle softness measured in ref 39 can play an additional role in the reduction of the structural order of the samples. We compared systems with similar number densities n since the addition of salt induces a progressive collapse of the DNA chains.[38] For consistency with the previous section, for all functionalities, we report a quantity proportional to n, the packing fraction calculated by assuming that the radius of the particles is equal to R, as measured in dilute conditions and without any added salt.

Figure 5a,b shows the radial distribution functions of the reference sample without added salt, and of samples with c = 0.05 and 1.00 M, for number densities that correspond to packing fractions η = 0.40 and 0.68 in the reference sample. Additional $g(r)$ functions for the remaining investigated packing fractions are reported in Figure S3 in the Supporting Information. Corresponding exemplary sample renderings are shown in Figure 5c, in which the particle color represents the value of the 6-fold order parameter. A strong reduction of the first and second peaks of the $g(r)$ is observed in both samples for c = 0.05 M. While the position of the first peak is comparable to that of the reference sample, the second peak

https://doi.org/10.1021/acs.macromol.2c00220
Macromolecules 2022, 55, 4459−4468

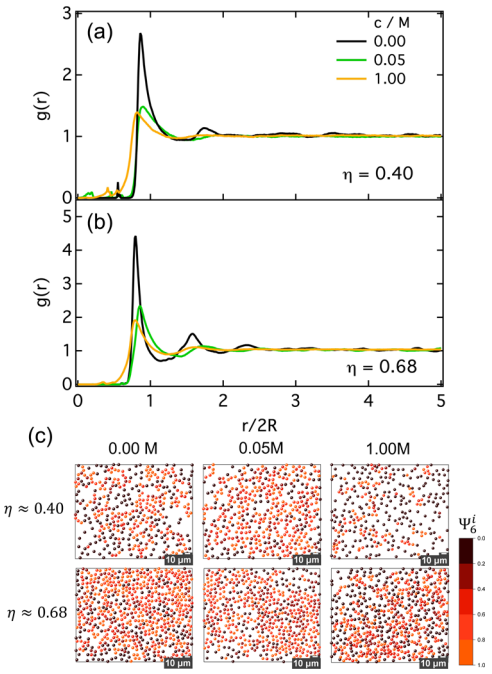

Figure 5. (a, b) Radial distribution function $g(r)$ for samples with different amounts of added salt (as indicated) and packing fraction η = 0.40 (a) and 0.68 (b). (c) Renderings of particle positions in samples with η = 0.40 and 0.68 and different amounts of added salt (as indicated). The particle color represents the value of the 6-fold order parameter, as indicated by the color scale.

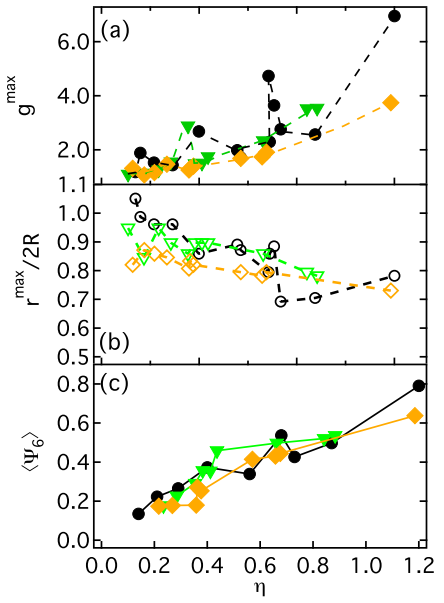

Figure 6. (a) Height and (b) position of the first peak of $g(r)$ and (c) average 6-fold order parameter $\langle\Psi_6\rangle$ as a function of η, for f = 1.0 × 10^5, N = 10 kbp, and salt concentrations c = 0.00 M (circles), c = 0.05 M (triangles down), and c = 1.00 M (Diamonds). Lines in (a) and (b) are a guide to the eye. Error bars are smaller than symbol sizes.

moves to larger distances, indicating a less compact second shell. This is confirmed by the snapshots in Figure 5c, in particular for η = 0.68, which show a more heterogeneous structure with larger interparticle distances. In addition, a significant reduction in the number of particles with large values of Ψ_6^i is also observed. These effects point to a reduction of the local order associated with less pronounced aggregation. One should consider that for c = 0.05 M, the reduction of particle size and the increase in particle softness is already significant and, in combination with DNA backfolding that reduces blunt-end induced attractions, might play an important role in decreasing the degree of average structural ordering. For the sample with c = 1.00 M, the reduction of the height of the peaks of the $g(r)$ is even larger and at the same time, the position of the first and second peaks moves to shorter distances. This can be associated with the pronounced reduction of particle size induced by the collapse of DNA fragments at such large values of c. The degree of local order is also reduced, as indicated by the smaller number of particles with large values of the order parameter. Similar to the case of the smaller functionality investigated, the peak of the $g(r)$ becomes broader, indicating the possible presence of a small degree of interdigitation.

Figure 6a shows the height of the first peak of $g(r)$, g^{max}, as a function of packing fraction for the three systems considered. For both salt concentrations, the reentrance observed for the case without added salt around η = 0.68 disappeared. Furthermore, for the system with c = 1.00 M, the peak height g^{max} increases more slowly with increasing η. Similarly, the dependence of the position of the first peak of $g(r)$, r^{max}, on η (Figure 6b) for the system with c = 0.05 M shows much less fluctuations and no sign of reentrance compared to the system without added salt. For the system with c = 1.00 M, an even smoother reduction is observed. For the reference system, the reduction of the peak position was explained in terms of the contribution to particle shrinkage coming from the pressure exerted by noncondensed counterions contained in the brushes of neighbor particles.

For c = 0.05 M, the counterion pressure contribution is reduced, but still present, as indicated by the slightly milder, but comparable dependence of r^{max} on η. Instead, for c = 1.00 M, all free counterions stay outside of the DNA brush and therefore the contribution disappears. The smoother reduction of the position for c = 1.00 M can be associated with the progressive crowding of the dispersion. The average 6-fold order parameter (Figure 6c) also shows a progressively smoother dependence on η with increasing salt concentration, especially for the case c = 1.00 M. The reduction of aggregation phenomena and the average degree of order with the addition of salt appears to be sharper than observed when changing the functionality: indeed already at the smallest salt concentration c = 0.025 M investigated in ref 37, aggregation already disappeared and the $g(r)$ was comparable to that reported here for c = 0.05 M. This supports the interpretation that in this case, beyond the reduction of blunt-end attractions due to DNA backfolding, the decrease of the particle size and the increase of particle softness additionally contribute to the observed trends.

The MSDs of the systems with different amounts of salt are compared in Figure 7a,b for the selected values of η = 0.40 and 0.68 (Figure S4 in the Supporting Information reports the MSDs of all investigated packing fractions).

For the two samples with added salt, a significant increase of the MSD is observed for both packing fractions, being more pronounced for c = 1.00 M. For η = 0.68, the dynamics of the salted systems are also qualitatively different, being diffusive (c = 1.00 M) or slightly subdiffusive (c = 0.05 M) in comparison to the slow, subdiffusive dynamics of the reference sample. The speedup of the dynamics with increasing salt concentration is

https://doi.org/10.1021/acs.macromol.2c00220
Macromolecules 2022, 55, 4459−4468

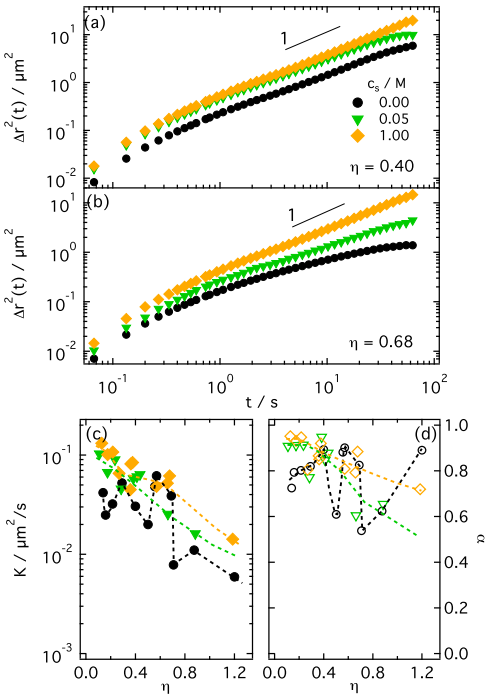

Figure 7. (a, b) Mean-square displacement $\Delta r^2(t)$ for samples with different amounts of added salt (as indicated) and packing fraction η = 0.40 (a) and 0.68 (b). (c, d) Transport coefficient K and exponent α obtained by fitting the long-time part of the MSD with a power law, $\Delta r^2(t) = 4Kt^{\alpha}$, as a function of η, different amounts of added salt, same (empty) symbols as in (c).

confirmed by the growth of the transport coefficient extracted from data obtained at all investigated packing fractions (Figure 7a). One can additionally see that the nonmonotonic trend associated with the aggregation induced by blunt-end attractions tends to disappear with the addition of salt. Similarly, the η dependence of the exponent α is smoother for c = 0.05 and 1.00 M and much more moderate for the largest salt content.

Summarizing, results on the structure and dynamics for increasing amount of added salt indicate a sudden disappearance of aggregation and the reduction of ordering, including the reentrance observed for the system without any added salt. These effects arise from the combination of the reduction of blunt-end attractions, induced by progressive DNA backfolding with increasing salt concentration, and the decrease of particle size and increase of particle softness.

Effect of Chain Length. The dependence of the structure and dynamics of the system on the DNA fragment length was investigated by considering salt-free dispersions of particles with $f = 2.5 \times 10^4$ and two different values N = 10 and 20 kbp. For these values of N, Figure 8a,b reports g^{max}, r^{max} (panels a and b), $\langle\Psi_6\rangle$ (panel c), K, and α (panels d and e) as a function of packing fraction η.

A smaller value of g^{max} is observed for the dispersions of particles with longer DNA fragments (Figure 8a) for $\eta \gtrsim 0.7$, indicating a smaller degree of ordering.

This is also confirmed by the smaller values of $\langle\Psi_6\rangle$ (Figure 8c). The reduced degree of order when reaching larger packing fractions could be an effect of the larger particle softness associated with the fact that longer DNA fragments form a less dense corona and are more flexible. It is interesting to note that a clear reentrance in the structure, indicated by the decrease of g^{max}, is observed for this system at packing fractions $\eta \approx 1.2$. At that packing fraction, also the order parameter saturates to about 0.6. Different effects might contribute to this disordering, like deswelling and/or deformation of the particles. Additionally, the reduction of r^{max} (Figure 8b) is significantly more pronounced than in the N = 10 kbp system, and at the maximum packing investigated, the minimal interparticle distance reduced to about 60% of the particle diameter (Figure 8b). The more pronounced reduction could be the

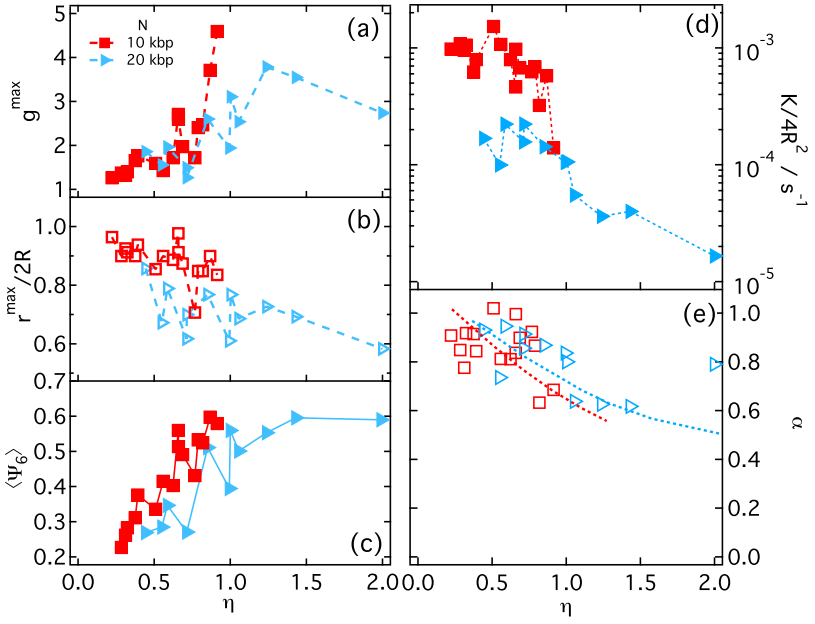

Figure 8. (a) Height and (b) position of the first peak of $g(r)$, (c) average 6-fold order parameter, (d) transport coefficient K, and (d) exponent α obtained by fitting the long-time part of the MSD with a power law, $\Delta r^2(t) = 4Kt^{\alpha}$, as a function of η, for N = 10 and 20 kbp (as indicated). Lines in (b) and (e) are a guide to the eye.

https://doi.org/10.1021/acs.macromol.2c00220
Macromolecules 2022, 55, 4459−4468

result of a stronger counterion-induced deswelling for the softer corona of the system with N = 20 kbp.

The values of K for samples with N = 20 kbp show a progressive reduction with a dependence on η similar to that of the samples with N = 10 kbp (Figure 8d). The transport coefficient of the samples with N = 20 kbp is however significantly smaller than that of samples with N = 10 kbp at a comparable packing fraction, even after normalization with the particle diameter squared (Figure 8d).

This suggests that the longer DNA chains have important effects on the hydrodynamics of the system, slowing down the particle displacements. This is in qualitative agreement with the corresponding slowdown of the dynamics with increasing particle functionality at fixed N. The exponents of the long-time part of the MSDs (Figure 8e) show a progressive transition from diffusion to subdiffusion, consistent with a dynamical arrest scenario. The exponents are comparable for the two values of N (Figure 8e).

CONCLUSIONS

The analysis of the microscopic structure and dynamics of increasingly packed quasi-2D dispersions of colloids grafted with long dsDNA fragments was used to investigate changes in the interactions of these systems associated with the functionality, the monovalent salt content, and the fragment length. Changes in the functionality and salinity have the effect of inducing a reduction and eventually complete disappearance of the aggregation phenomena and the nonmonotonic ordering associated with the presence of attractive interactions between the blunt-end of dsDNA fragments. In the case of functionality, while DNA presents in all cases a stretched configuration with the consequence that the majority of blunt-end are located on the external surface of the corona, the reduction in their density leads to a reduction of the effective attractive interaction between colloids. These results thus confirm that both the dsDNA fragment configuration and a sufficiently large surface density of blunt-end are needed to generate significant attraction between the colloids. In the case of salinity, a reduction of attraction is also expected due to the salt-induced DNA backfolding,[38] which reduces the probability of direct interaction between the blunt-end of neighbor DNA brushes. However, additional effects might play an important role in this case: the progressive reduction of particle size and the softening of the brush. This possibly leads to a sharper reduction of aggregation phenomena and reentrant ordering in this case. In parallel, the dsDNA fragment length can be used as an additional parameter to tune the softness of the particles and thus again the interactions, with important effects on large packing fractions where particle deswelling and deformation play an important role. The fragment length induces also changes in the dynamics, which go beyond the effect associated with the size increase and could be possibly linked to hydrodynamics.

Our study determines the conditions under which blunt-end base stacking interactions induce an effective attraction between spherical dsDNA brushes and provides simple and precise means of controlling them during synthesis (changes in functionality and fragment length) or dispersion preparation (salt content). Fine control of these parameters can be used to guide colloidal assembly through blunt-end interactions, which to date have been mainly exploited in DNA nanotechnology but provide a valuable parallel route to assembly mechanisms using base pairing. The control of the attraction intensity described before could be combined with a control of the spatial location of grafting and the sequence of the DNA primers such as to add directionality control on the interactions. The realization of particles with directional blunt-end interactions could allow the assembly of colloidal materials with desired photonic[48,49] and plasmonic properties.[50,51] Additional parameters potentially influencing the blunt-end interactions and therefore assembly, like temperature, are still to be explored.

ASSOCIATED CONTENT

Supporting Information

The Supporting Information is available free of charge at https://pubs.acs.org/doi/10.1021/acs.macromol.2c00220.

Radial distribution functions and mean-square displacements for $f = 25 \times 10^4$ and 5×10^3 under salt-free conditions; radial distribution functions and mean-squared displacements for $f = 1.0 \times 10^5$, 1 and 0.05 M of NaCl; and radial distribution functions and mean-square displacements for $f = 2.5 \times 10^4$ and fragment length N = 20 kbp under salt-free conditions (PDF)

AUTHOR INFORMATION

Corresponding Author

Marco Laurati − *Dipartimento di Chimica & CSGI, Università di Firenze, 50019 Sesto Fiorentino, Italy;* orcid.org/0000-0003-1334-5940; Email: marco.laurati@unifi.it

Authors

Ivany C. Romero-Sanchez − *División de Ciencias e Ingenierías, Universidad de Guanajuato, 47150 León, Mexico; Dipartimento di Chimica & CSGI, Università di Firenze, 50019 Sesto Fiorentino, Italy*

Laura E. Castellano − *División de Ciencias e Ingenierías, Universidad de Guanajuato, 47150 León, Mexico;* orcid.org/0000-0002-0969-3128

Complete contact information is available at: https://pubs.acs.org/10.1021/acs.macromol.2c00220

Author Contributions

I.C.R.-S. prepared samples, performed experiments, and analyzed the data. M.L. and L.E.C. instructed on sample preparation and experimental techniques and provided materials. M.L. designed the research. All authors interpreted the results and wrote the paper. The manuscript was written through contributions of all authors. All authors have given approval to the final version of the manuscript.

Funding

Conacyt, "Consorzio per lo Sviluppo dei Sistemi a Grande Interfase" (CSGI),

Notes

The authors declare no competing financial interest.

ACKNOWLEDGMENTS

The authors thank E. Stiakakis, C. N. Likos, R. Castañeda-Priego, R. Moctezuma-Martiñon, and E. Zaccarelli for fruitful discussions. I.C.R.-S., L.E.C., and M.L. acknowledge Conacyt for funding through grant A1-S-9098. M.L. and I.C.R.-S. acknowledge financial support from "Consorzio per lo Sviluppo dei Sistemi a Grande Interfase" (CSGI).

REFERENCES

(1) Seeman, N. C.; Sleiman, H. F. DNA Nanotechnology. *Nat. Rev. Mater.* **2018**, *3*, No. 17068.
(2) Chidchob, P.; Sleiman, H. F. Recent Advances in DNA Nanotechnology. *Curr. Opin. Chem. Biol.* **2018**, *46*, 63−70.
(3) Lohse, S. E.; Murphy, C. J. Applications of Colloidal Inorganic Nanoparticles: From Medicine to Energy. *J. Am. Chem. Soc.* **2012**, *134*, 15607−15620.
(4) Klinkova, A.; Choueiri, R. M.; Kumacheva, E. Self-Assembled Plasmonic Nanostructures. *Chem. Soc. Rev.* **2014**, *43*, 3976−3991.
(5) Kuzyk, A.; Schreiber, R.; Fan, Z.; Pardatscher, G.; Roller, E.-M.; Högele, A.; Simmel, F. C.; Govorov, A. O.; Liedl, T. DNA-Based Self-Assembly of Chiral Plasmonic Nanostructures with Tailored Optical Response. *Nature* **2012**, *483*, 311−314.
(6) Ma, W.; Xu, L.; de Moura, A. F.; Wu, X.; Kuang, H.; Xu, C.; Kotov, N. A. Chiral Inorganic Nanostructures. *Chem. Rev.* **2017**, *117*, 8041−8093.
(7) Li, N.; Tittl, A.; Yue, S.; Giessen, H.; Song, C.; Ding, B.; Liu, N. DNA-Assembled Bimetallic Plasmonic Nanosensors. *Light Sci. Appl.* **2014**, *3*, e226.
(8) Tibbitt, M. W.; Dahlman, J. E.; Langer, R. Emerging Frontiers in Drug Delivery. *J. Am. Chem. Soc.* **2016**, *138*, 704−717.
(9) Walsh, A. S.; Yin, H.; Erben, C. M.; Wood, M. J. A.; Turberfield, A. J. DNA Cage Delivery to Mammalian Cells. *ACS Nano* **2011**, *5*, 5427−5432.
(10) Hamblin, G. D.; Carneiro, K. M. M.; Fakhoury, J. F.; Bujold, K. E.; Sleiman, H. F. Rolling Circle Amplification-Templated DNA Nanotubes Show Increased Stability and Cell Penetration Ability. *J. Am. Chem. Soc.* **2012**, *134*, 2888−2891.
(11) Jensen, S. A.; Day, E. S.; Ko, C. H.; Hurley, L. A.; Luciano, J. P.; Kouri, F. M.; Merkel, T. J.; Luthi, A. J.; Patel, P. C.; Cutler, J. I.; Daniel, W. L.; Scott, A. W.; Rotz, M. W.; Meade, T. J.; Giljohann, D. A.; Mirkin, C. A.; Stegh, A. H. Spherical Nucleic Acid Nanoparticle Conjugates as an RNAi-Based Therapy for Glioblastoma. *Sci. Transl. Med.* **2013**, *5*, No. 209ra152.
(12) Fakhoury, J. J.; McLaughlin, C. K.; Edwardson, T. W.; Conway, J. W.; Sleiman, H. F. Development and Characterization of Gene Silencing DNA Cages. *Biomacromolecules* **2014**, *15*, 276−282.
(13) Bujold, K. E.; Fakhoury, J.; Edwardson, T. G. W.; Carneiro, K. M. M.; Briard, J. N.; Godin, A. G.; Amrein, L.; Hamblin, G. D.; Panasci, L. C.; Wiseman, P. W.; Sleiman, H. F. Sequence-Responsive Unzipping DNA Cubes with Tunable Cellular Uptake Profiles. *Chem. Sci.* **2014**, *5*, 2449−2455.
(14) Burns, J. R.; Seifert, A.; Fertig, N.; Howorka, S. A Biomimetic DNA-Based Channel for the Ligand-Controlled Transport of Charged Molecular Cargo across a Biological Membrane. *Nat. Nanotechnol.* **2016**, *11*, 152−156.
(15) Czogalla, A.; Franquelim, H. G.; Schwille, P. DNA Nanostructures on Membranes as Tools for Synthetic Biology. *Biophys. J.* **2016**, *110*, 1698−1707.
(16) Kallenbach, N. R.; Ma, R.-I.; Seeman, N. C. An Immobile Nucleic Acid Junction Constructed from Oligonucleotides. *Nature* **1983**, *305*, 829−831.
(17) Rothemund, P. W. K. Folding DNA to Create Nanoscale Shapes and Patterns. *Nature* **2006**, *440*, 297−302.
(18) Wei, B.; Dai, M.; Yin, P. Complex Shapes Self-Assembled from Single-Stranded DNA Tiles. *Nature* **2012**, *485*, 623−626.
(19) McLaughlin, C. K.; Hamblin, G. D.; Sleiman, H. F. Supramolecular DNA Assembly. *Chem. Soc. Rev.* **2011**, *40*, 5647−5656.
(20) Kwak, M.; Herrmann, A. Nucleic Acid Amphiphiles: Synthesis and Self-Assembled Nanostructures. *Chem. Soc. Rev.* **2011**, *40*, 5745−5755.
(21) Woo, S.; Rothemund, P. W. K. Programmable Molecular Recognition Based on the Geometry of DNA Nanostructures. *Nat. Chem.* **2011**, *3*, 620−627.
(22) Nakata, M.; Zanchetta, G.; Chapman, B. D.; Jones, C. D.; Cross, J. O.; Pindak, R.; Bellini, T.; Clark, N. A. End-to-End Stacking and Liquid Crystal Condensation of 6− to 20−Base Pair DNA Duplexes. *Science* **2007**, *318*, 1276−1279.
(23) Rogers, W. B.; Shih, W. M.; Manoharan, V. N. Using DNA to Program the Self-Assembly of Colloidal Nanoparticles and Microparticles. *Nat. Rev. Mater.* **2016**, *1*, No. 16008.
(24) Michele, L. D.; Di Eiser, E. Developments in Understanding and Controlling Self Assembly of DNA-Functionalized Colloids. *Phys. Chem. Chem. Phys.* **2013**, *15*, 3115−3129.
(25) Nykypanchuk, D.; Maye, M. M.; van der Lelie, D.; Gang, O. DNA-Guided Crystallization of Colloidal Nanoparticles. *Nature* **2008**, *451*, 549−552.
(26) Biancaniello, P. L.; Kim, A. J.; Crocker, J. C. Colloidal Interactions and Self-Assembly Using DNA Hybridization. *Phys. Rev. Lett.* **2005**, *94*, No. 58302.
(27) Park, S. Y.; Lytton-Jean, A. K. R.; Lee, B.; Weigand, S.; Schatz, G. C.; Mirkin, C. A. DNA-Programmable Nanoparticle Crystallization. *Nature* **2008**, *451*, 553−556.
(28) Casey, M. T.; Scarlett, R. T.; Benjamin Rogers, W.; Jenkins, I.; Sinno, T.; Crocker, J. C. Driving Diffusionless Transformations in Colloidal Crystals Using DNA Handshaking. *Nat. Commun.* **2012**, *3*, No. 1209.
(29) Soto, C. M.; Srinivasan, A.; Ratna, B. R. Controlled Assembly of Mesoscale Structures Using DNA as Molecular Bridges. *J. Am. Chem. Soc.* **2002**, *124*, 8508−8509.
(30) Schade, N. B.; Holmes-Cerfon, M. C.; Chen, E. R.; Aronzon, D.; Collins, J. W.; Fan, J. A.; Capasso, F.; Manoharan, V. N. Tetrahedral Colloidal Clusters from Random Parking of Bidisperse Spheres. *Phys. Rev. Lett.* **2013**, *110*, No. 148303.
(31) Di Michele, L.; Varrato, F.; Kotar, J.; Nathan, S. H.; Foffi, G.; Eiser, E. Multistep Kinetic Self-Assembly of DNA-Coated Colloids. *Nat. Commun.* **2013**, *4*, No. 2007.
(32) Tan, S. J.; Kahn, J. S.; Derrien, T. L.; Campolongo, M. J.; Zhao, M.; Smilgies, D.-M.; Luo, D. Crystallization of DNA-Capped Gold Nanoparticles in High-Concentration, Divalent Salt Environments. *Angew. Chem., Int. Ed.* **2014**, *53*, 1316−1319.
(33) Cheng, W.; Hartman, M. R.; Smilgies, D.-M.; Long, R.; Campolongo, M. J.; Li, R.; Sekar, K.; Hui, C.-Y.; Luo, D. Probing in Real Time the Soft Crystallization of DNA-Capped Nanoparticles. *Angew. Chem., Int. Ed.* **2010**, *49*, 380−384.
(34) Rajendran, A.; Endo, M.; Katsuda, Y.; Hidaka, K.; Sugiyama, H. Programmed Two-Dimensional Self-Assembly of Multiple DNA Origami Jigsaw Pieces. *ACS Nano* **2011**, *5*, 665−671.
(35) Salamonczyk, M.; Zhang, J.; Portale, G.; Zhu, C.; Kentzinger, E.; Gleeson, J. T.; Jakli, A.; De Michele, C.; Dhont, J. K. G.; Sprunt, S.; Stiakakis, E. Smectic Phase in Suspensions of Gapped DNA Duplexes. *Nat. Commun.* **2016**, *7*, No. 13358.
(36) Gerling, T.; Wagenbauer, K. F.; Neuner, A. M.; Dietz, H. Dynamic DNA Devices and Assemblies Formed by Shape-Complementary, Non−Base Pairing 3D Components. *Science* **2015**, *347*, 1446−1452.
(37) Romero-Sanchez, I.; Pihlajamaa, I.; Adžić, N.; Castellano, L. E.; Stiakakis, E.; Likos, C. N.; Laurati, M. Blunt-End Driven Re-Entrant Ordering in Quasi Two-Dimensional Dispersions of Spherical DNA Brushes. *ACS Nano* **2022**, *16*, 2133−2146.
(38) Zhang, J.; Lettinga, P. M.; Dhont, J. K. G.; Stiakakis, E. Direct Visualization of Conformation and Dense Packing of DNA-Based Soft Colloids. *Phys. Rev. Lett.* **2014**, *113*, No. 268303.
(39) Moreno-Guerra, J. A.; Romero-Sánchez, I. C.; Martinez-Borquez, A.; Tassieri, M.; Stiakakis, E.; Laurati, M. Model-Free Rheo-AFM Probes the Viscoelasticity of Tunable DNA Soft Colloids. *Small* **2019**, *15*, No. 1904136.
(40) de With, A.; Greulich, K. O. Wavelength Dependence of Laser-Induced DNA Damage in Lymphocytes Observed by Single-Cell Gel Electrophoresis. *J. Photochem. Photobiol., B* **1995**, *30*, 71−76.
(41) Repula, A.; Oshima Menegon, M.; Wu, C.; van der Schoot, P.; Grelet, E. Directing Liquid Crystalline Self-Organization of Rodlike Particles through Tunable Attractive Single Tips. *Phys. Rev. Lett.* **2019**, *122*, No. 128008.

https://doi.org/10.1021/acs.macromol.2c00220
Macromolecules 2022, 55, 4459−4468

(42) Sbalzarini, I. F.; Koumoutsakos, P. Feature Point Tracking and Trajectory Analysis for Video Imaging in Cell Biology. *J. Struct. Biol.* **2005**, *151*, 182−195.
(43) Tinevez, J.-Y.; Perry, N.; Schindelin, J.; Hoopes, G. M.; Reynolds, G. D.; Laplantine, E.; Bednarek, S. Y.; Shorte, S. L.; Eliceiri, K. W. TrackMate: An Open and Extensible Platform for Single-Particle Tracking. *Methods* **2017**, *115*, 80−90.
(44) Li, L.; Pabit, S. A.; Lamb, J. S.; Park, H. Y.; Pollack, L. Closing the Lid on DNA End-to-End Stacking Interactions. *Appl. Phys. Lett.* **2008**, *92*, No. 223901.
(45) Maffeo, C.; Luan, B.; Aksimentiev, A. End-to-End Attraction of Duplex DNA. *Nucleic Acids Res.* **2012**, *40*, 3812−3821.
(46) Kilchherr, F.; Wachauf, C.; Pelz, B.; Rief, M.; Zacharias, M.; Dietz, H. Single-Molecule Dissection of Stacking Forces in DNA. *Science* **2016**, *353*, No. aaf5508.
(47) Kanayama, N.; Sekine, T.; Ozasa, K.; Kishi, S.; Nyu, T.; Hayashi, T.; Maeda, M. Terminal-Specific Interaction between Double-Stranded DNA Layers: Colloidal Dispersion Behavior and Surface Force. *Langmuir* **2016**, *32*, 13296−13304.
(48) Kuzyk, A.; Jungmann, R.; Acuna, G. P.; Liu, N. DNA Origami Route for Nanophotonics. *ACS Photonics* **2018**, *5*, 1151−1163.
(49) Steckl, A. J. DNA − a New Material for Photonics? *Nat. Photonics* **2007**, *1*, 3−5.
(50) Chao, J.; Lin, Y.; Liu, H.; Wang, L.; Fan, C. DNA-Based Plasmonic Nanostructures. *Mater. Today* **2015**, *18*, 326−335.
(51) Liu, N.; Liedl, T. DNA-Assembled Advanced Plasmonic Architectures. *Chem. Rev.* **2018**, *118*, 3032−3053.

https://doi.org/10.1021/acs.macromol.2c00220
Macromolecules 2022, 55, 4459−4468